ADVANCED OPTICAL MATERIALS
www.advopticalmat.de

Coherent Control of the Nonlinear Emission of Single Plasmonic Nanoantennas by Dual-Beam Pumping

Agostino Di Francescantonio, Andrea Locatelli, Xiaofei Wu, Attilio Zilli, Thorsten Feichtner, Paolo Biagioni, Lamberto Duò, Davide Rocco, Costantino De Angelis, Michele Celebrano, Bert Hecht, and Marco Finazzi*

The control of nonlinear optical signals in nanostructured systems is pivotal to develop functional devices suitable for integration in optical platforms. A possible control mechanism is exploiting coherent interactions between different nonlinear optical processes. Here, this concept is implemented by taking advantage of the strong field enhancement and high optical nonlinearity provided by plasmonic nanostructures. Two beams, one at the angular frequency ω, corresponding to the telecom wavelength $\lambda = 1551$ nm, and the other at 2ω, are combined to generate a sum-frequency signal at 3ω from single asymmetric gold nanoantennas. This nonlinear signal interferes with the third-harmonic radiation generated by the beam at ω, resulting in a modulation up to 50% of the total signal at 3ω depending on the relative phase between the beams. Such a large intensity modulation of the nonlinear signal is accompanied by a rotation of its polarization axis, due to the lack of central symmetry of the nanostructure. The demonstration that the nonlinear emission can be coherently controlled through the phase difference of the two-color illumination represents a promising route toward all-optical logic operations at the nanoscale through nonlinear optical signal manipulation.

1. Introduction

In the last decade, nonlinear optics underwent a huge renewal of interest thanks to the steady development of nanostructured materials and metamaterials.[1] In such systems,[2] exploiting the huge local field enhancement associated with their electromagnetic modes, it has been demonstrated that it is possible to attain sizable nonlinear signals albeit the volume of matter involved is very small and the nonlinear multiphoton interaction has a perturbative character. Moreover, by engineering the electromagnetic modes of the nanostructure, the nonlinear signal can be efficiently coupled with radiative modes.[3] Various material platforms have been proposed to implement these concepts. Among them, noble metals can produce intense local fields thanks to lightning rod effects exalted by the plasmonic resonances of the nanostructure.[4] Plasmonic nanoantennas were indeed among the first examples of structured systems for nanoscale nonlinear optics; their bulk third-order nonlinearity was exploited for third-harmonic generation (THG)[5] and four-wave mixing (FWM).[6,7] Because of the centrosymmetric lattice, however, even-order nonlinear bulk susceptibilities in these materials commonly vanish.[8] Yet, even-order processes like second-harmonic generation (SHG) are still possible thanks to the symmetry breaking introduced by the metal–environment interface and to the strong field gradients caused by the finite penetration depth.[9,10] Nevertheless, great care is needed to design a plasmonic antenna geometry that exploits such large even-order nonlinear surface susceptibilities.[11] For instance, the geometry of the nanostructure should lack an inversion center to avoid destructive interference of the nonlinear radiation in the far field.[12] A general requirement for optimizing both even and odd nonlinear optical processes consists in achieving mode-matching conditions, which correspond to the spatial and spectral overlap of resonating modes at the excitation and emission wavelengths.[13,14] In this way, the plasmon enhancement is exploited to increase both the pump incoupling and the emission outcoupling.[15]

In previous works, we applied this concept to V-shaped nanostructures coupled with nanorods, boosting the efficiency of

A. Di Francescantonio, A. Zilli, T. Feichtner, P. Biagioni, L. Duò, M. Celebrano, M. Finazzi
Physics Department
Politecnico di Milano
Milano 20133, Italy
E-mail: michele.celebrano@polimi.it

A. Locatelli, D. Rocco, C. De Angelis
Department of Information Engineering
University of Brescia
Brescia 25123, Italy

X. Wu, T. Feichtner, B. Hecht
Nano-Optics and Biophotonics Group, Experimental Physics 5
University of Würzburg
97074 Würzburg, Germany

The ORCID identification number(s) for the author(s) of this article can be found under https://doi.org/10.1002/adom.202200757.

DOI: 10.1002/adom.202200757

both SHG and THG processes.[16,17] Doubly resonant designs can be very effective also to optimize multiple frequency excitation, boosting both $\chi^{(2)}$ and $\chi^{(3)}$ wave-mixing processes, as demonstrated, for instance, by gold nanowires displaying a multiresonant behavior, which led to efficient FWM.[18] Signatures of sum-frequency generation (SFG) were also found in the THG emission of the already mentioned V-shaped antennas, with a significant contribution from a cascade process mediated by SHG.[17] Wave-mixing processes in nanostructured systems have been exploited for sensing and spectroscopy,[19] and for realizing tunable light sources.[20] Moreover, the introduction of a second excitation channel allows the implementation of an ultrafast all-optical control of the nonlinear signal, as e.g. in Ref. [21]. Another recent example is represented by the symmetry-enabled polarization control of the nonlinear signal in atomically thin semiconductors through degenerate double-pump excitation.[22] A further possibility for tuning the nonlinear signal with dual beam excitation lies in the coherent interaction between different nonlinear processes that produce outputs at the same wavelength. A comparable scheme was already proposed to control the light scattering from a single nanostructure by means of SHG.[23] Along this line, we have recently investigated the interaction between degenerate SFG and THG conversion processes in AlGaAs nanoresonators.[24] However, because of the cylindrical geometry of the nanostructures, the coherent interaction practically vanished, so that only the sum of the individual contributions was measured. Following the same idea, in this work we investigate the SFG process in *asymmetric* doubly-resonant plasmonic nanoantennas. In particular, we address the wave-mixing process in which two beams, one at the angular frequency ω and the other at 2ω, are combined to generate a SFG signal at 3ω, where ω corresponds to the telecom wavelength $\lambda = 1551$ nm. We observe non-trivial interactions in the nonlinear emission related to the frequency degeneracy of the SFG with the THG excited by the pump at ω, extremely sensitive to the specific geometric parameters of the nanoantenna under investigation. Our results demonstrate the possibility, offered by the asymmetry of the nanostructure, to perform a two-pump coherent control of the nonlinear emission through the interference between SFG and THG. Bringing such process to the nanoscale could pave the way for applications ranging from optical signal processing to bio-imaging and optical communication.[25–27]

2. $\omega + 2\omega$ Sum-Frequency Generation

We experimentally investigate SFG and THG by dual-pump excitation on non-centrosymmetric gold nanoantennas (**Figure 1**a). The fabrication process of the nanoantennas is thoroughly described elsewhere.[16] Such antennas show a resonance (V_1 in Figure 1b) at the telecom wavelength 1551 nm. This resonance stems from oscillating currents within the V-shaped substructure that lead to a dipolar moment, excited with an electric field oscillating along the y direction, as indicated in Figure 1a. Shorter wavelength resonances originate instead from dipole charge oscillations within either the V-shaped or rod substructure, which are only excited by light linearly polarized along the x axis of Figure 1a.[16] These resonances hybridize to form bonding and antibonding modes, visible in Figure 1b

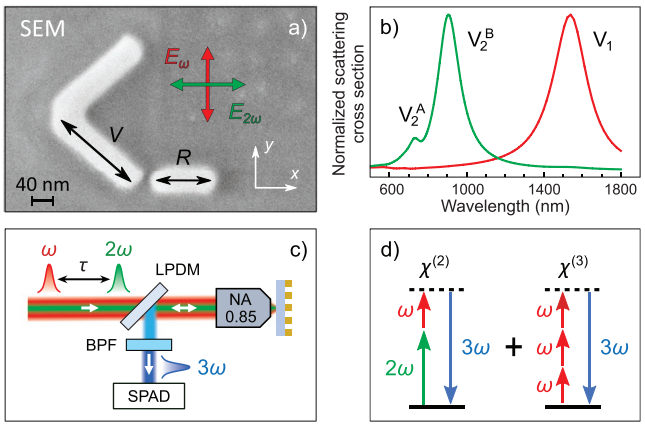

Figure 1. a) Scanning electron micrograph of a representative non-centrosymmetric V-antenna. The red and green arrows represent the polarization of the excitation at ω and 2ω, respectively. V and R indicate the lengths of the V-shaped substructure and of the rod. b) Simulated scattering cross-section spectrum. The two modes V_1 and $V_2^{A,B}$ (A and B standing for "antibonding" and "bonding", respectively) are excited by light linearly polarized along either the x (green line) or the y (red line) direction. c) Setup of the experiment. Here, τ is the relative delay between the pulses, LPDM is a long-pass mirror, BPF is a band-pass filter centered at 517 nm, SPAD is a single-photon avalanche diode and NA = 0.85 is the objective numerical aperture. d) Energy diagrams illustrating the two nonlinear processes that produce a signal at 3ω: $\chi^{(2)}$-mediated SFG ($3\omega = \omega + 2\omega$) and $\chi^{(3)}$-mediated THG ($3\omega = \omega + \omega + \omega$).

as feature V_2^B and V_2^A, respectively. Our design aims at overlapping V_1 with the wavelength of the ω beam, and mode V_2^A with the wavelength of the 2ω one.[16,17] Several nanostructures with varying V and R geometrical parameters (see Figure 1a) are fabricated in square arrays with 3 μm lateral spacing. This ensures the absence of near-field coupling between the nanostructures and allows one to address individual antennas, since it is much larger than the lateral resolution of our microscope objective. As reported in Ref. [16], the double resonance condition described above is met for $V \simeq 180$ nm and $R \simeq 120$ nm.

A simplified sketch of the experimental apparatus, thoroughly described elsewhere,[24] is depicted in Figure 1c (see also the Experimental Section). Two-color excitation is achieved by partial frequency doubling of the light from a pulsed laser. The two beams are separated by a dichroic mirror in the two arms of an interferometer, where one pulse is retarded by a delay line. The two beams are then recombined and fed into a dry microscope objective with numerical aperture NA = 0.85. The nonlinear signal is collected by the same objective in backscattering, filtered by a band-pass filter centered at 517 nm, and detected by a single-photon avalanche diode (SPAD).

Since the 2ω beam is obtained as the double-frequency replica of the beam at ω, the SFG process at 3ω is intrinsically degenerate with the THG one, associated with the upconversion of three ω photons (Figure 1d). Note also that mode matching in these nanoantennas is achieved only for the excitation fields, since no resonant feature appears at 3ω (i.e. $\lambda = 517$ nm).

2.1. Interference

The frequency-degenerate THG and SFG contributions can be disentangled by analyzing the dependence of the nonlinear

output signal on the time delay τ between the ω and 2ω beams. Given a temporal duration of the ω pulse $\tau_\omega = 160$ fs, for $|\tau| \gg \tau_\omega$ the delay trace (see an example in **Figure 2**a) shows a baseline that is ascribed to the pure THG excited at ω. When $|\tau|$ becomes comparable or smaller than the pulse duration, and the polarizations of ω and 2ω beams impinging on the nanoantenna are cross-polarized and aligned as indicated in Figure 1a, the delay trace shows an additional feature associated with the SFG process, which produces interference fringes with the THG signal. We would like to stress that no significant SFG signal is conversely observed for different polarizations of the exciting beams (see Figure S2 in Section S3 of the Supporting Information). By restricting the analysis around $|\tau| \approx 0$, one can better appreciate the periodic oscillations of the 3ω signal due to SFG–THG interference (see Figure 2b).

Delay traces can be described by the following analytical expression of the power $W_{3\omega}$ of the 3ω signal, which explicitly accounts for the coherent superposition of the SFG and THG signals in the far field as a function of the delay (see derivation in Section S2, Supporting Information).

$$W_{3\omega} = W_{\mathrm{THG}} + W_{\mathrm{SFG}}\left(2^{-\frac{16\tau^2}{3\sigma^2}}\right) + \gamma\sqrt{W_{\mathrm{THG}}W_{\mathrm{SFG}}}\left(2^{-\frac{16\tau^2}{3\sigma^2}}\right)\cos(2\tau\omega) \quad (1)$$

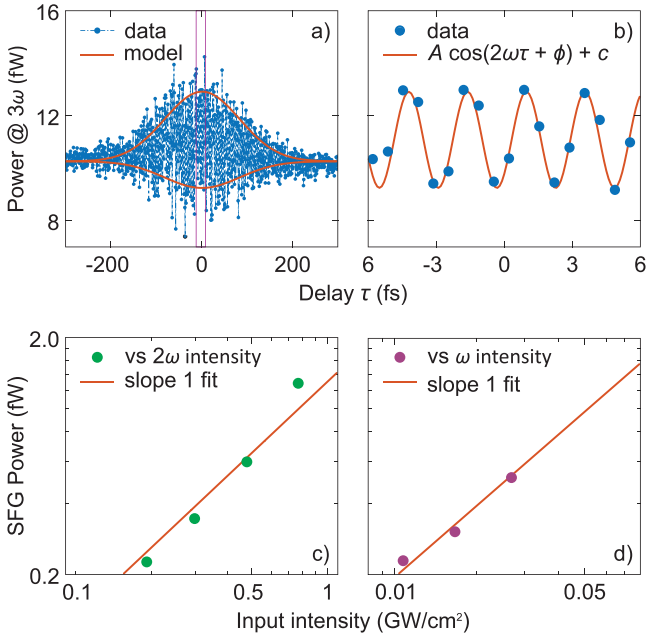

Figure 2. a) Delay trace recorded on an antenna with $V = 175$ nm and $R = 105$ nm. Data obtained with ω and 2ω beam intensity equal to 30 and 500 MW cm^{-2}, respectively. The red solid lines represent the envelope of the interference fringes, obtained by fitting the data with Equation 1 and then setting $\cos(2\tau\omega) = \pm 1$. b) Zoom of panel a around the zero-delay condition to highlight the interference fringes (the purple box in panel (a)). c) The red line is the best fit to the data obtained with the function $A\cos(2\omega\tau + \phi) + c$ by varying the amplitude A, the phase ϕ and the offset c. d) Dependence of the power of the SFG signal extracted from the delay curves (see text) on the pump power. The power of either pump beam is varied by keeping the other one constant (with the same intensity of panels (a) and (b)). The solid lines are linear fits to the data with slope constrained to 1. The data have been recorded on the antenna with $V = 175$ nm and $R = 145$ nm.

In this expression, W_{THG} and W_{SFG} are the powers of the THG and SFG signals (the latter evaluated at zero delay time), respectively, while σ is the full-width-at-half-maximum duration of the 1551 nm pulse (which, for simplicity, is approximated with a Gaussian lineshape). We can separate a THG baseline and a Gaussian envelope that describes the interference. Note that a possible (although extremely unlikely, see the Experimental Section) leakage of unfiltered ω and 2ω photons in the signal would only provide a delay-independent, additional background, not affecting the extrapolation of the SFG signal from the delay traces. The parameter γ, which may vary between 0 and 1, accounts for the interference between the SFG and THG fields averaged over the solid angle of collection, defined by the numerical aperture of the objective (see the Section S2, Supporting Information). Our model expressed by Equation (1) is validated by observing that in Figure 2b the 3ω signal oscillates with an angular frequency equal to 2ω as a function of the delay τ and in Figure 2a the FWHM of the Gaussian envelope matches well the temporal cross-correlation between the ω and 2ω pulses ($\approx$ 195 fs). The dynamic range spanned by the pump powers is limited to about one decade, on the lower end by the sensitivity of the SPAD, on the higher end by the damage threshold of the nanoantenna. Nevertheless, by fitting the experimental interferograms using Equation (1), we are able to disentangle W_{THG} and W_{SFG}. As shown in Figure 2c,d, the latter scales linearly with the power of both pumps as expected from SFG, confirming the validity of the fitting approach and the SFG character of the process. Conversely, the dependence of the delay-independent background on the ω beam intensity is cubic (not shown), as expected for THG emission and reported in Ref. [17].

From Figure 2a, one can observe that the SFG and THG interference can result in very large modulations of the 3ω signal. We would like to stress that this is due to the lack of central symmetry of the investigated nanoantennas. In fact, in centro-symmetric structures and axial illumination/collection geometry, one should expect $\gamma = 0$, as discussed in Ref. [24], and no interference fringes should be observed. The detection of such fringes goes far beyond being a mere side effect of the frequency degeneracy between SFG and THG. Instead, it offers an opportunity to coherently modulate the nonlinear signal by dephasing the input pulses. This represents an alternative route to coherent control with respect to Ref. [28], where THG was interferentially modulated by dephasing two pump beams that selectively excited different but "frequency degenerate surface plasmon polaritons modes in the same nanostructure". In the example reported in Figure 2a, a $\tau \simeq 1.5$ fs delay produces a variation almost by a factor of 2 of the 3ω signal, from 3.5 to 6.5 kcounts s^{-1}. Such coherent modulation is attainable thanks to the fast electron-mediated nonlinear interaction of the two pumps, which exploits virtual intermediate states in the optical transitions. This allows an ultrafast control of the signal over a fs time scale. Conversely, a phonon-mediated nonlinear process would result in much longer relaxation times.

2.2. Polarization Properties

The reduced symmetry of the nanostructure is reflected also in the polarization properties of the nonlinear signal emitted

at 2ω and 3ω.[16,17] In particular, the polarization of the THG field (reported in Table S1, Supporting Information) reveals next to the direct, $\chi^{(3)}$-mediated THG a significant contribution of a cascade process seeded by $\chi^{(2)}$-mediated SHG, consisting in a first SHG step ($\omega + \omega = 2\omega$) followed by a SFG step ($\omega + 2\omega = 3\omega$). Note that this cascaded THG pathway does not require an external beam at 2ω.[17,29] The polarization state of the cascaded THG emission of non-centrosymmetric gold nanoantennas directly reflects the asymmetric distribution of second-harmonic fields within the structure, resulting in a tilted polarization axis of the THG radiation with respect to the linear polarization of the pump beam at ω.[17] Controlling the currents oscillating within the antenna at 2ω with an external beam is therefore expected to provide additional control also of the polarization of the 3ω signal, besides its intensity.

The polarization state of the 3ω signal is analyzed by a polarizer placed in front of the SPAD unit when the sample is illuminated with ω and 2ω beams polarized along y and x, respectively (see **Figure 3**a). To separate the THG and SHG contributions, we first measure the THG signal by blocking the 2ω beam, then we subtract it from the 3ω signal obtained when both ω and 2ω impinge on the sample and average over several interference fringes in an interval around $\tau = 0$ to cancel out the interference term. The results are reported in the polar plots of Figure 3b. To better highlight the effects of $\omega + 2\omega$ SFG on the output polarization, the $\theta_{det} = 0$ angle has been chosen *along* the THG polarization axis. A further tilt of the SFG polarization axis with respect to the THG is observed, as shown in Figure 3b, where the additional tilt is ≈30°. This behavior is qualitatively well reproduced (see Figure 3c) by nonlinear finite-element simulations performed by using COMSOL Multiphysics, which confirm that $\chi^{(2)}$-mediated SFG introduces a tilt in the 3ω polarization. Albeit the simulated tilt is less than the one observed in the experiment, the qualitative agreement is remarkable, considered the fact that nonlinear optical simulations are extremely sensitive to the chosen $\chi^{(2)}$ value and to the field distribution inside the structures. Moreover, an approach to SFG based on a surface $\chi^{(2)}$ susceptibility might underestimate other SFG mechanisms that could be relevant at the nanoscale.

3. Effect of the Geometry

The dimensions of each substructure of non-centrosymmetric antennas influence the spectral position of the plasmonic resonances of the overall structure (see Section S1, Supporting Information) but also affect the antenna radiation pattern. As a result, both SFG and THG strongly depend on the nanoantenna geometry. In **Figures 4**a–d are plotted the delay traces recorded on antennas in which the V-arm length V is varied from 135 to 195 nm in steps of 20 nm, while the rod length R is kept fixed at 105 nm. These traces show different THG baselines superimposed with a more or less pronounced bell-shaped SFG-related feature. The most efficient antenna for both THG and SFG is the one with the resonance V_1 of the V-substructure matched with ω, corresponding to V = 175 nm. The interferometric visibility depends on the powers W_{SFG} and W_{THG}, being maximum for similar THG and SFG powers (Figure 4c), confirming the possibility of performing a large coherent modulation on such asymmetric nanostructures.

Analytical traces obtained after fitting the corresponding experimental ones with Equation (1) are plotted in Figures 4e–h. The retrieved parameter γ, defined in Section 2, shows great variability between different geometries. In particular, we observe the maximum\γ value for the most resonant structure (i.e. for V = 175 nm). To assess the influence of the geometry on the interference, we analyzed the far-field emission of the antennas

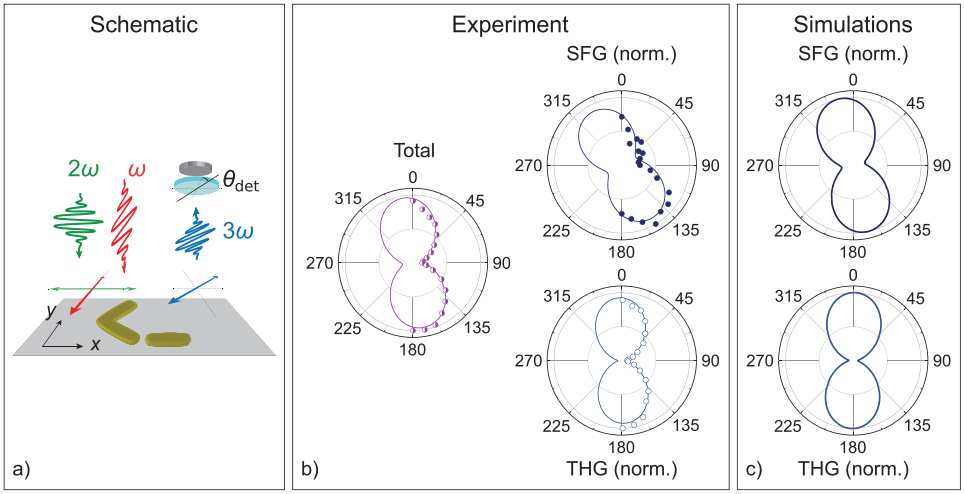

Figure 3. a) Sketch of the polarization-resolved measurement. The antenna is excited by cross-polarized pumps with ω and 2ω beam intensity equal to 30 and 500 MW cm^{-2}, respectively. The signal at 3ω passes through a polarization analyzer before being detected by the photon counter. b) Polar plots measured at 3ω from an antenna with V = 175 nm and R = 105 nm. The solid lines are fitting functions of the form $B \sin^2(\theta_{det} + \psi)$, B and ψ being free parameters. The total signal has been recorded by averaging the interference fringes of a delay trace near the zero-delay condition. The SFG power is then obtained by subtracting the THG power (recorded previously by blocking the beam at 2ω) from the resulting signal. All the polar plots are normalized to the maximum. The $\theta_{det} = 0$ condition corresponds to the angle that maximizes the THG signal. The intensity ratio from SFG over THG powers is 0.25 (taken at $\theta_{det} = 0$). c) Simulated polar plots for the same antenna geometry as in panel (b).

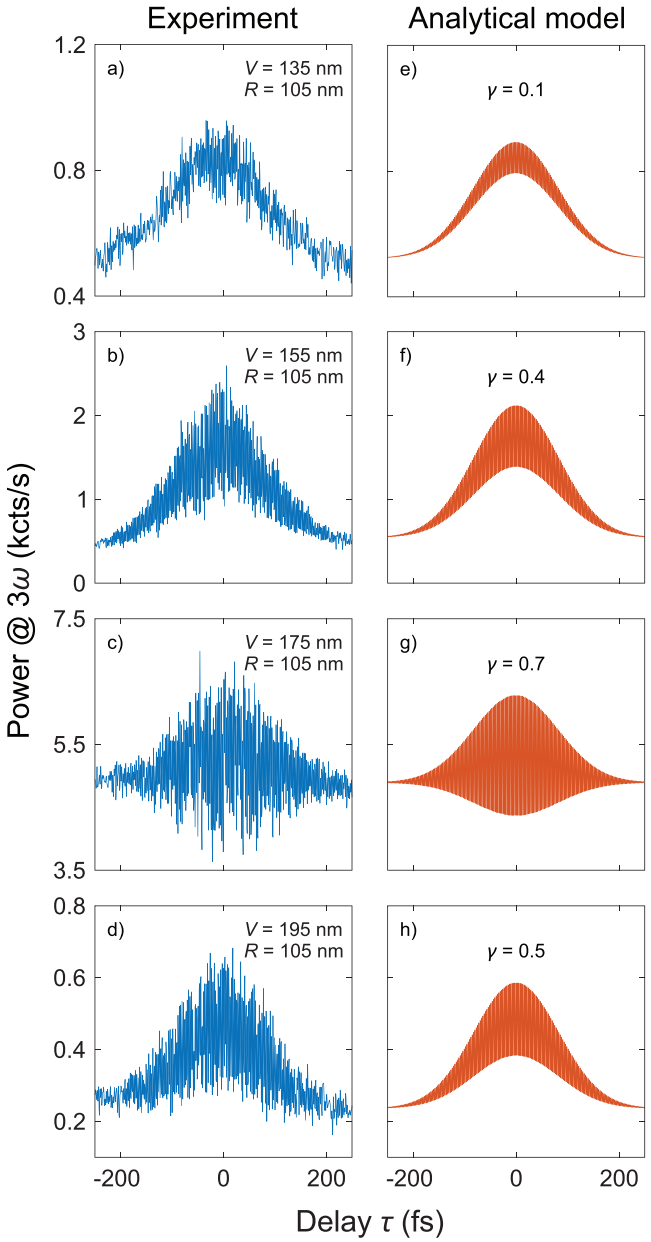

Figure 4. a–d) Delay traces from four nanoantennas with the same rod length $R = 105$ nm and variable V arm length V, as indicated in each panel. The time-averaged power of both the ω and the 2ω pump beam is 50 µW before the objective, corresponding to an intensity on the sample of 30 and 500 MW cm^{-2}, respectively. The delay step is 0.66 fs. Analytical fits with Equation (1) of the corresponding experimental traces. The fitting values of (W_{THG}, W_{SFG}) in kcts s^{-1} are e) (0.52, 0.32), f) (0.48, 1.16), g) (4.89, 0.40), and h) (0.25, 0.25). The values of γ are indicated in each panel.

by means of BFP simulations. The distribution of the THG and SFG fields is reported for two antenna geometries in **Figure 5**. The asymmetric field distribution reflects the lack of inversion symmetry of the investigated nanostructures and is essential to avoid the perfect cancellation of SFG+THG interference effects.[24] We evaluated the analytical expression of γ (Equation S6, Supporting Information) within the portion of back focal plane limited by the objective NA (the green circle in

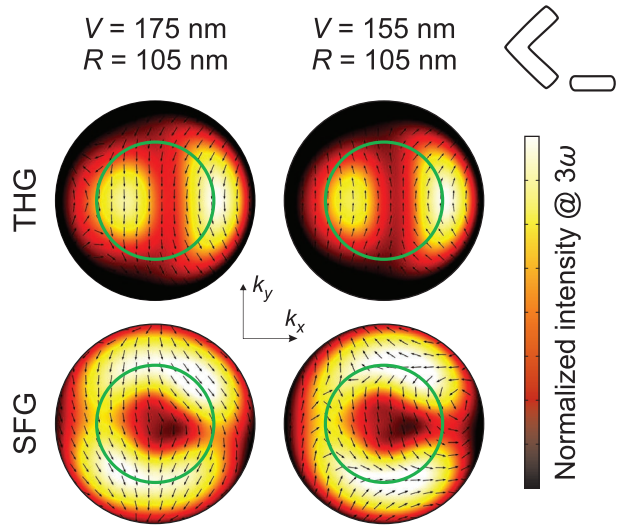

Figure 5. Back focal plane maps of the nonlinear emission, for two geometries, identified by the (V, R) parameters. The intensity of THG and SFG is plotted in color scale. The arrows indicate the electric field direction. The green circles define the solid angle of detection defined by the objective numerical aperture. On the top right is indicated the orientation of the nanostructure with respect to the plots.

Figure 5). The arrow fields in Figure 5 display a shift of almost π of the THG phase far from resonance, which brings it in antiphase with the SFG field, thus reducing the value of γ. The calculated values of γ (see Section S4, Supporting Information) show a trend that reproduces qualitatively what is observed in Figure 4e–h. From Figure 5 one can notice that SFG and THG field distributions in the back focal plane show non-parallel polarizations, which limits the maximum interference between the two components. Large values of modulation in terms of γ can nevertheless be obtained, especially for resonant antennas.

The THG and SFG powers W_{THG} and W_{SHG} extrapolated by fitting with Equation (1) are plotted in **Figure 6** as a function of both the V-arm and the rod length and compared to nonlinear finite-element simulations. According to the linear properties of the nanostructure (see Figure S1, Supporting Information), the resonance V_1 at ω disperses strongly with V. This brings about a strong resonant behavior of the THG (Figure 6a–c), due to its characteristic dependence $|E(\omega)|^3$, whereas the linear dependence of SFG (Figure 6b–d) means a less sensitive dependence on V. As for R, it mainly affects the resonance V_2^A at 2ω, as a consequence of the hybridization of the rod resonance with the second resonance of the V-substructure. Therefore, R barely influences the THG, whereas it strongly affects the SFG.

The polarization analysis of the total 3ω signal emitted by antennas with different combinations of the V and R parameters is reported in **Figure 7**. All the investigated antennas display a variable tilt $\theta_{3\omega}$ of the polarization ruled by the SFG contribution to the total signal. In the most resonant antennas ($V = 175$ nm), we find a small rotation of the overall polarization, due to the prominence of the THG with respect the SFG. Conversely, when the SFG signal is comparatively larger we detect an extra tilt of the total 3ω signal. As mentioned in Section 2, the tilt angles are referenced to the THG polarization. The

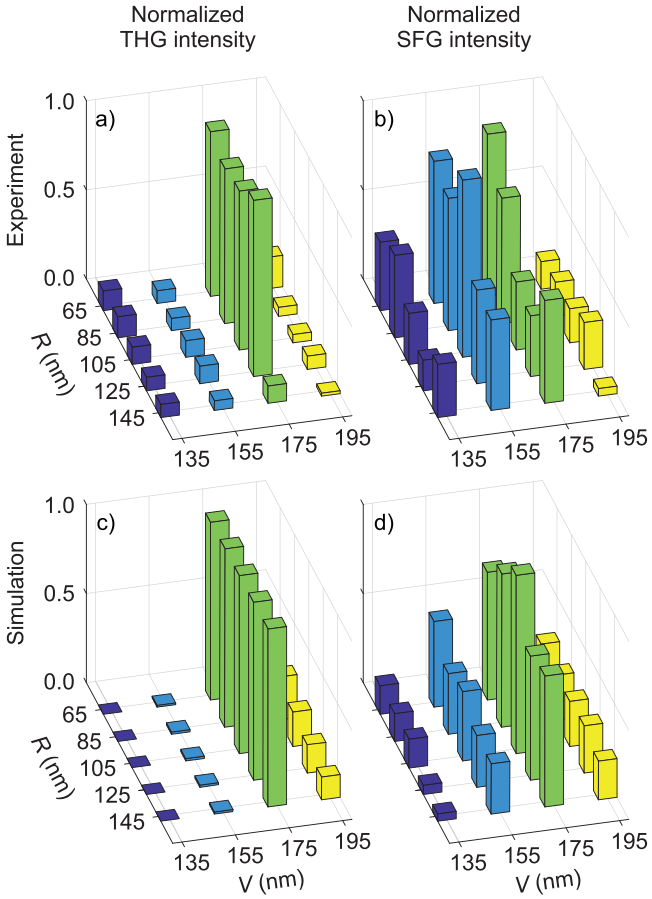

Figure 6. Dependence of the measured a) THG and b) SFG emitted power on the geometric parameters V and R of the nanoantennas. The SFG data are obtained by fitting the delay traces with Equation (1). c) THG and d) SFG signals computed with nonlinear finite-element simulations.

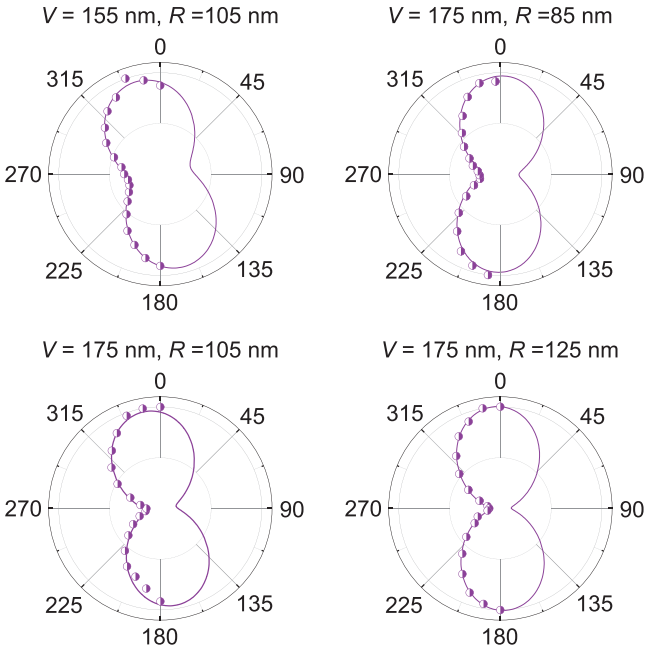

Figure 7. Polarization of the overall 3ω signal from selected nanoantennas. The polar plots are labelled with the geometrical parameters of the nanoantennas, namely V and R. The plotted data represent the total signal (THG and SFG) recorded by averaging the fringes over a small temporal window around the $\tau \simeq 0$ condition (average over about 20 fringes). Data are obtained with ω and 2ω beam intensity equal to 30 and 500 MW cm^{-2}, respectively. The $\theta_{det} = 0$ direction is the polarization of the THG signal obtained by blocking the 2ω beam. The solid lines are fitting functions of the form $B\sin^2(\theta_{det} + \theta_{3\omega})$, B and $\theta_{3\omega}$ being free parameters. The values of polarization tilts $\theta_{3\omega}$ retrieved by the fits are provided in the Table S1.

measured absolute angles are provided in the section S5 (Supporting Information).

4. Conclusion

We have investigated the SFG process obtained by a two-color excitation of asymmetric plasmonic antennas exhibiting resonances at both pump frequencies. In particular, we adopted a ω–2ω pump configuration, where one exciting beam was obtained by externally doubling the frequency of the other beam. The resulting $\chi^{(2)}$-mediated SFG signal at 3ω is therefore degenerate in frequency and coherent with the THG produced by the nanostructures thanks to the $\chi^{(3)}$ bulk susceptibility of the gold nanoantenna. Far from being a nuisance, the degeneracy between the THG and SFG results in large interference modulations (up to a factor of 2) of the 3ω signal upon small variations of the phase difference between the ω and 2ω beams, enabling a coherent control of the amplitude of the 3ω emission. The intrinsic ultrafast nature of the nonlinear interaction can be an asset to implement a fast control of the signal by simply changing the relative phase between the pumps. The lack of central symmetry of the investigated nanostructures also results in differing polarization properties of the SFG and THG emission. This suggests that not only the amplitude but also the polarization of the nonlinear emission at 3ω can be coherently controlled with a two-color illumination, disclosing multiple routes for nonlinear all-optical signal manipulation at the nanoscale.

The relatively low nonlinear signal strength of a single nanoantenna could be compensated by exploiting a periodic ensemble of identical meta-atoms produced by scalable lithography techniques. In such a platform, constructive interference between the nonlinear signals coherently generated by all the illuminated structures would produce a nonlinear diffraction pattern with intensities in the diffraction spots scaling as the square of the number of elements in the array. This would bring applications such as encoding information with high bit rate or ultrafast optical switching within reach.

5. Experimental Section

Experimental Setup: The laser source was an Er:Yb:glass mode-locked laser (OneFive, Origami 15-80) characterized by a 160 fs pulse duration, an 80 MHz repetition rate, and an operation wavelength $\lambda = 1551$ nm. The second pulse at $\lambda/2$=775.5 nm was obtained by frequency doubling the pulse at 1551 nm in a beta-barium borate (BBO) crystal. A dichroic mirror separated the ω pulse from the 2ω one and the latter was

subsequently retarded by a delay stage (Physik Instrumente, M-404). The two beams were then recombined and focused on the sample by an 0.85 NA objective (Nikon, CFI Plan Fluor 60XC). The sample was placed on an *xyz*-piezo-electric stage (Physik Instrumente, P-517.3CL) and was excited from the glass substrate side. The nonlinear signal was collected by the same objective in a backscattering configuration and was detected with a single-photon avalanche diode (Micro Photon Devices, PD-050-CTD) after being spectrally filtered in a narrow band $\approx \lambda/3 = 518$ nm (Thorlabs, FESH0700 + FBH520-40) for further rejection of the ω and 2ω reflected radiation. According to the specifications provided by the manufacturer, the combination of the long-pass dichroic mirror and the band-pass filter (respectively indicated as LPCD and BPF in Figure 1c) ensured a transmission $<10^{-16}$ of the 2ω pump beam. On the other hand, the photon energy of the ω pump beam fell within the energy gap of our SPAD and, therefore, could not be detected. A simplified diagram of the experimental set-up (not including the polarization optics) can be found in Figure S1 (Supporting Information) of Ref. [24].

Numerical Simulations: Nonlinear finite-element simulations were performed by employing the commercial software Comsol Multiphysics. The details of the numerical simulations and the values of the employed nonlinear susceptibilities are the same as those reported in Ref. [17]. A perturbative approach based on the so-called undepleted pump approximation was applied. First, the linear behavior of the nanostructures at the ω and 2ω pump frequencies was evaluated with plane-wave illumination. Then, the nonlinear currents at 3ω due to bulk third-order nonlinearity of gold and to surface second-order nonlinearity at gold–dielectric interfaces were calculated by using fields from the previous step, and used as source terms to study THG and SFG, respectively. Cascade effects represented a non-negligible contribution to the overall THG. However, the tilt they introduced in the THG polarization angle were of the order of few degrees.[17] Since the simulations aim to reproduce the "qualitative" trends of the polarization patterns observed with dual beam excitation, for the sake of simplicity cascade effects were neglected in the numerical modeling of the total THG signal.

Supporting Information

Supporting Information is available from the Wiley Online Library or from the author.

Acknowledgements

The authors acknowledge financial support from the European Union's Horizon 2020 Research and Innovation program "METAFAST" (Grant agreement No. 899673) and from the Italian Ministry of University and Research through the PRIN project NOMEN (2017MP7F8F). This project has also received funding from the European Union's Horizon 2020 research and innovation programme under the Marie Skłodowska-Curie scheme (Grant agreement No. 837928).

Open Access Funding provided by Politecnico di Milano within the CRUI-CARE Agreement.

Conflict of Interest

The authors declare no conflict of interest.

Data Availability Statement

The data that support the findings of this study are available from the corresponding author upon reasonable request.

Keywords

nanoantennas, nonlinear optics, plasmonics, sum-frequency generation, third-harmonic generation

Received: March 31, 2022
Revised: May 12, 2022
Published online:

[1] L. Bonacina, P.-F. Brevet, M. Finazzi, M. Celebrano, *J. Appl. Phys.* **2020**, *127*, 230901.
[2] L. Novotny, N. van Hulst, *Nat. Photonics.* **2011**, *5*, 83.
[3] T. Feichtner, S. Christiansen, B. Hecht, *Phys. Rev. Lett.* **2017**, *119*, 217401.
[4] M. Kauranen, A. V. Zayats, *Nat. Photonics.* **2012**, *6*, 737.
[5] M. Lippitz, M. A. van Dijk, M. Orrit, *Nano Lett.* **2005**, *5*, 799.
[6] M. Danckwerts, L. Novotny, *Phys. Rev. Lett.* **2007**, *98*, 026104.
[7] T. Hanke, G. Krauss, D. Träutlein, B. Wild, R. Bratschitsch, A. Leitenstorfer, *Phys. Rev. Lett.* **2009**, *103*, 257404.
[8] R. Boyd, *Nonlinear optics*, Academic Press, an imprint of Elsevier, London **2020**.
[9] G. Bachelier, J. Butet, I. Russier-Antoine, C. Jonin, E. Benichou, P.-F. Brevet, *Phys. Rev. B* **2010**, *82*, 235403.
[10] J. Butet, P.-F. Brevet, O. J. F. Martin, *ACS Nano* **2015**, *9*, 10545.
[11] N. C. Panoiu, W. E. I. Sha, D. Y. Lei, G.-C. Li, *J. Opt.* **2018**, *20*, 083001.
[12] M. Finazzi, P. Biagioni, M. Celebrano, L. Duò, *Phys. Rev. B* **2007**, *76*, 125414.
[13] K. Thyagarajan, S. Rivier, A. Lovera, O. J. F. Martin, *Opt. Express* **2012**, *20*, 12860.
[14] D. Vercruysse, Y. Sonnefraud, N. Verellen, F. B. Fuchs, G. D. Martino, L. Lagae, V. V. Moshchalkov, S. A. Maier, P. V. Dorpe, *Nano Lett.* **2013**, *13*, 3843.
[15] K.-Y. Yang, J. Butet, C. Yan, G. D. Bernasconi, O. J. F. Martin, *ACS Photonics* **2017**, *4*, 1522.
[16] M. Celebrano, X. Wu, M. Baselli, S. Großmann, P. Biagioni, A. Locatelli, C. De Angelis, G. Cerullo, R. Osellame, B. Hecht, L. Duò, F. Ciccacci, M. Finazzi, *Nat. Nanotechnol.* **2015**, *10*, 412.
[17] M. Celebrano, A. Locatelli, L. Ghirardini, G. Pellegrini, P. Biagioni, A. Zilli, X. Wu, S. Grossmann, L. Carletti, C. De Angelis, L. Duò, B. Hecht, M. Finazzi, *Nano Lett.* **2019**, *19*, 7013.
[18] H. Harutyunyan, G. Volpe, R. Quidant, L. Novotny, *Phys. Rev. Lett.* **2012**, *108*, 217403.
[19] D. Lis, Y. Caudano, M. Henry, S. Demoustier-Champagne, E. Ferain, F. Cecchet, *Adv. Opt. Mater.* **2013**, *1*, 244.
[20] Y. Zhang, A. Manjavacas, N. J. Hogan, L. Zhou, C. Ayala-Orozco, L. Dong, J. K. Day, P. Nordlander, N. J. Halas, *Nano Lett.* **2016**, *16*, 3373.
[21] G. Sartorello, N. Olivier, J. Zhang, W. Yue, D. J. Gosztola, G. P. Wiederrecht, G. Wurtz, A. V. Zayats, *ACS Photonics* **2016**, *3*, 1517.
[22] S. Klimmer, O. Ghaebi, Z. Gan, A. George, A. Turchanin, G. Cerullo, G. Soavi, *Nat. Photonics* **2021**, *15*, 837.
[23] S. G. Rodrigo, H. Harutyunyan, L. Novotny, *Phys. Rev. Lett.* **2013**, *110*, 177405.
[24] A. Zilli, D. Rocco, M. Finazzi, A. Di Francescantonio, L. Duò, C. Gigli, G. Marino, G. Leo, C. De Angelis, M. Celebrano, *ACS Photonics* **2021**, *8*, 1175.
[25] R. Camacho-Morales, L. Xu, N. Dimitrov, L. Stoyanov, Z. Ma, A. A. Dreischuh, H. H. H. Tan, C. De Angelis, C. Jagadish,

A. E. Miroshnichenko, D. Rocco, V. F. Gili, A. Komar, M. Lysevych, F. Karouta, G. Leo, M. Rahmani, D. N. Neshev, *Adv. Photonics* **2021**, *3*, 036002.

[26] G. Marino, A. S. Solntsev, L. Xu, V. F. Gili, L. Carletti, A. N. Poddubny, M. Rahmani, D. A. Smirnova, H. Chen, A. Lemaître, G. Zhang, A. V. Zayats, C. De Angelis, G. Leo, A. A. Sukhorukov, D. N. Neshev, *Optica* **2019**, *6*, 1416.

[27] G. Campargue, L. L. Volpe, G. Giardina, G. Gaulier, F. Lucarini, I. Gautschi, R. L. Dantec, D. Staedler, D. Diviani, Y. Mugnier, J.-P. Wolf, L. Bonacina, *Nano Lett.* **2020**, *20*, 8725.

[28] F. Zeuner, M. Muldarisnur, A. Hildebrandt, J. Förstner, T. Zentgraf, *Nano Lett.* **2015**, *15*, 4189.

[29] S. D. Gennaro, C. F. Doiron, N. Karl, P. P. Iyer, D. K. Serkland, M. B. Sinclair, I. Brener, *ACS Photonics* **2022**, *9*, 1026.